PCCP

ROYAL SOCIETY OF CHEMISTRY

PAPER

View Article Online
View Journal | View Issue

Cite this: *Phys. Chem. Chem. Phys.*, 2024, **26**, 22882

Temperature-driven journey of dark excitons to efficient photocatalytic water splitting in β-AsP†

Harshita Seksaria, Amal Kishore and Abir De Sarkar *

Received 9th May 2024,
Accepted 24th June 2024

DOI: 10.1039/d4cp01937g

rsc.li/pccp

Limited availability of photogenerated charge carriers in two-dimensional (2D) materials, due to high exciton binding energies, is a major bottleneck in achieving efficient photocatalytic water splitting (PWS). Strong excitonic effects in 2D materials demand precise attention to electron–electron correlation, electron–hole interaction and electron–phonon coupling simultaneously. In this work, we explore the temperature-dependent electronic and optical responses of an efficient photocatalyst, blue-AsP (β-AsP), by integrating electron–phonon coupling into state-of-the-art GW + BSE calculations. Interestingly, strong electron-lattice interaction at high temperature promotes photocatalytic water splitting with an increasing supply of long-lived dark excitons. This work presents an atypical observation contrary to the general assumption that only bright excitons enhance the PWS due to prominent absorption. Dark excitons, due to the low recombination rate, exhibit long-lived photogenerated electron–hole pairs with high exciton lifetime increasing with temperature up to ∼0.25 μs.

1. Introduction

While the high-temperature optical properties have gained recognition for their substantial technological significance across diverse fields,[1–3] their potential in photocatalytic applications remains largely unexplored. In photocatalytic water splitting, the catalyst plays a vital role by absorbing light and generating electron–hole pairs (excitons) that migrate to the catalyst-water interface and drive the redox reactions. It is well established that temperature affects the redox reactions in photocatalysis.[4–7] However, the effect of temperature on excitonic and optical responses remains ripe for investigation.

Two-dimensional materials exhibit rich optical spectra with numerous bright and dark excitons, which offer significant potential if effectively regulated. The exciton energies resulting from electron–hole interactions are determined as the eigen energies of an excitonic Hamiltonian or, more precisely, as the solution to a Bethe–Salpeter equation (BSE) describing the correlation function for the two particles.[8] Heine, Allen, and Cardona (HAC) highlighted many years ago[9,10] that the electron–phonon coupling can cause electronic level corrections of comparable magnitude to those brought about by electron–electron correlation. Yet, the number of studies employing first-principles methods and calculations to investigate this issue has been notably scarce. As temperature increases, the atoms in a material vibrate more intensely. This thermal motion disrupts the orderly arrangement of atoms and affects the electronic energy states, ultimately influencing the way light interacts with the material and, therefore, the optical and electronic properties of the material. Therefore, understanding the intricate interplay between electron–electron correlation, electron–hole interaction, and electron–phonon coupling is now crucial to explaining the temperature-dependent evolution of optoelectronic properties in 2D materials. Most theoretical studies on 2D material excitonic properties still rely on simplistic models like the Mott–Wannier model, which inadequately capture electron–hole interactions. Implementing GW + BSE alone is complex, yet crucial for accurate electron–hole interaction representation. Incorporating electron–phonon coupling atop GW + BSE becomes even more challenging but essential for studying phonon-assisted electronic and optical properties.

The optical properties of metals are well-understood,[11–14] but semiconductors present more formidable challenges due to various interacting particles and their intricate behavior.[15,16] This difficulty increases even more in two-dimensional systems due to reduced dimensionality and quantum confinement. Although few recent studies have incorporated electron–phonon coupling in dielectric properties,[16–18] the ability to fully control exciton behaviour remains elusive. This necessitates a thorough investigation comprising the temperature-mediated influence of lattice interactions, the dynamics of excitons, including their binding energy and lifetime, as well as the electronic and optical responses of the material. The absence of a comprehensive and rigorous first-principles approach in this domain serves as motivation for us to explore optical and excitonic processes mediated by both

Institute of Nano Science and Technology, Knowledge City, Sector 81, Manauli, Mohali, Punjab 140306, India. E-mail: abir@inst.ac.in, abirdesarkar@gmail.com

† Electronic supplementary information (ESI) available. See DOI: https://doi.org/10.1039/d4cp01937g

electrons and phonons, considering temperature variations in general semiconductors.

The renormalization of eigen energies of electrons resulting from the interaction of electrons with the lattice is primarily done with either of the three key first principles techniques: (i) the path-integral molecular dynamics (PIMD) method, (ii) the Allen–Heine–Cardona (AHC) formalism, or (iii) the frozen phonon approach.[19] AHC theory, based on the rigid-ion approximation, incorporates the second-order derivative of the eigen energies as a critical component. Through a consolidated temperature-dependent AHC approach derived entirely from first principles for both electrons and phonons, we examine the full-spectrum dielectric function in blue arsenic phosphide (β-AsP), a promising and efficient emerging photocatalyst[20–30] and investigate four crucial parameters in the arsenal of photocatalytic water splitting: band gap, exciton binding energy, exciton lifetime, and optical spectra. The blue-AsP monolayer facilitates water oxidation and hydrogen reduction half reactions in both acidic and neutral media at distinct active sites. When exposed to light, it efficiently produces direct H_2, without needing additional cocatalysts or sacrificial reagents, from both clean (pH = 7) and acidic water (pH = 0). In a recent study, we investigated the behaviour of excited excitons in β-AsP, focusing on how to manipulate their binding energy and spatial separation.[31]

In this study, we explore the influence of electron-lattice interaction on the electronic, optical and excitonic properties of blue-AsP at various temperatures by integrating electron–phonon coupling into the state-of-the-art GW + BSE calculations. The optical properties thus calculated show strong excitonic effects, with a diverse range of tightly bound dark and bright excitons contributing to a complex picture. While the conventional assumption is that only brightly emitting excitons contribute to photocatalytic water splitting (PWS) due to their strong absorption, we demonstrate that the prominent availability of dark excitons can significantly promote photocatalysis with impressively high exciton lifetime. Long-lived excitons not only enhance photocatalytic activity by suppressing electron–hole recombination and increasing the probability of exciton dissociation,[32,33] but also offer exciting possibilities for manipulation in external electromagnetic fields, opening avenues for novel excitonic devices.[34–37]

2. Methods

The calculations based on first principles were executed using density functional theory (DFT)[38] *via* the Vienna *ab initio* simulation package (VASP).[39,40] Projected augmented wave (PAW) was used to depict the interactions between electrons and ions.[41] For the calculations of the exchange–correlation functionals, we employed the GGA-PBE (generalized gradient approximation of the Perdew–Burke–Ernzerhof) method.[42] To address the underestimation of the bandgap by PBE and ensure accurate computation of electronic properties, the screened hybrid HSE06 (Heyd–Scuseria–Ernzerhof 2006)[43] was utilized. This involved substituting a quarter of the exchange interaction from GGA-PBE with that of the HSE06 functionals. For the purpose of wave function expansion, we set an energy threshold at 500 eV, and we allowed both atoms and the unit cell to fully relax until the Hellmann–Feynman forces were reduced to below 0.001 eV $Å^{-1}$. We established the convergence criteria at 10^{-8} eV for self-consistent calculations. The Brillouin zone was sampled using a Γ-centered k-mesh of dimensions 18 × 18 × 1. We introduced a vacuum buffer of about 24 Å in the z-direction to restrict any interactions due to periodic replications. Phonon dispersion curves were derived using density functional perturbation theory (DFPT) integrated into the PHONOPY[44] software, applied on a 5 × 5 × 1 k-mesh within a 6 × 6 × 1 supercell that contains 72 atoms.

For optical analyses, the ground-state wave functions were determined using DFT, with the GGA-PBE functional as incorporated in the Quantum ESPRESSO software.[45] The interactions between ions and electrons were modelled using norm-conserving pseudopotentials,[46] sourced from the SG15 library,[47] without the non-linear core correction (NLCC). The non-local part of the pseudopotentials is also incorporated in our optical calculations.[48] A plane-wave basis was used to expand the electronic wavefunctions with a cutoff energy of 50 Ry, ensuring a total energy convergence of 1×10^{-6} Ry per atom. A dense k-mesh grid is required for precise optical calculations. Convergence was achieved using a 17 × 15 × 1 grid within the Bethe Salpeter equation (BSE) framework. We executed the optical calculations using the Yambo code[49,50] grounded in the random phase approximation (RPA) theory, including local field effects and extended by leveraging the Bethe Salpeter equation (BSE) atop G_0W_0, taking into account the intricacies of electron–hole interaction dynamics. The static screening analysis took into account 40 bands, of which 30 were unoccupied. To construct the exchange component of the BSE kernel that incorporates local field effects, 11 609 G-vectors were utilized for the Hartree potential. Additionally, a block size of 4 Ry for the screened interaction, relevant to the electron–hole interaction, was found to be optimally convergent. Furthermore, to include electron-lattice interactions, we employ a dynamic extension of the static Rayleigh–Schrödinger perturbation theory of electron–phonon coupling within the framework of the AHC theory[9,51] as incorporated in Yambo code. Within this framework, the quasiparticle (QP) energies are identified as the complex poles of the Green's function, expressed in relation to the electron–phonon (EP) self-energy, denoted as $\sum_{nk}^{\text{el-ph}}(\omega, T)$. This self-energy comprises two components: the Fan term $\sum_{nk}^{\text{FAN}}(\omega, T)$, and the Debye–Waller term $\sum_{nk}^{\text{DW}}(T)$.[52,53]

$$\sum_{n\mathbf{k}}^{\text{FAN}}(i\omega, T) = \sum_{n'\mathbf{q}\lambda} \frac{\left|g^{\mathbf{q}\lambda}_{nn'\mathbf{k}}\right|^2}{N_q} \times \left[\frac{N_{\mathbf{q}\lambda}(T) + 1 - f_{n'\mathbf{k}-\mathbf{q}}}{i\omega - \varepsilon_{n'\mathbf{k}-\mathbf{q}} - \omega_{\mathbf{q}\lambda}} + \frac{N_{\mathbf{q}\lambda}(T) + f_{n'\mathbf{k}-\mathbf{q}}}{i\omega - \varepsilon_{n'\mathbf{k}-\mathbf{q}} + \omega_{\mathbf{q}\lambda}}\right] \quad (1)$$

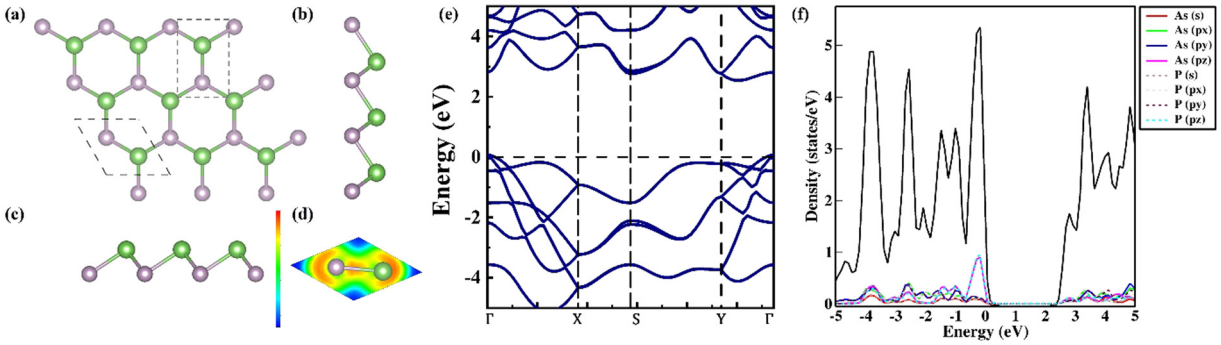

Fig. 1 Geometrical structure of blue-AsP: (a) top view, (b) and (c) side view, (d) electron localization function (ELF) plot; (e) electronic band structure using the HSE06 functional and (f) partial density of states plot.

$$\sum_{n\mathbf{k}}^{\mathrm{DW}}(T) = -\frac{1}{2N_q}\sum_{\mathbf{q}\lambda}\frac{\Lambda^{\mathbf{q}\lambda}_{nn'\mathbf{k}}}{\varepsilon_{n'\mathbf{k}} - \varepsilon_{n\mathbf{k}}}\left(2N_{\mathbf{q}\lambda}(T)+1\right) \tag{2}$$

where $N_{\mathbf{q}\lambda}(T)$ represents the Bose distribution function of the phonon mode $(\mathbf{q},\lambda)$ at the temperature T, and $\omega_{\mathbf{q}\lambda}$ are the phonon frequencies, while $g^{q,\lambda}_{nn'k}$ and $\Lambda^{q\lambda}_{nn'k}$ are the first order derivative EP matrix elements.

The frequency-dependent optical absorption $\alpha(\omega)$, refractive index $n(\omega)$ and extinction coefficient $\kappa(\omega)$ spectra were obtained using the full-spectrum dielectric function $\varepsilon(\omega) = \varepsilon_1(\omega) + i\varepsilon_2(\omega)$ with the following relations:

$$\alpha(\omega) = \sqrt{2}\omega\left\{\sqrt{\varepsilon_1^2(\omega)+\varepsilon_2^2(\omega)} - \varepsilon_1(\omega)\right\}^{\frac{1}{2}} \tag{3}$$

$$n(\omega) = \sqrt{\frac{\sqrt{\varepsilon_1^2(\omega)+\varepsilon_2^2(\omega)}+\varepsilon_1(\omega)}{2}} \tag{4}$$

$$\kappa(\omega) = \sqrt{\frac{-\varepsilon_1(\omega)+\sqrt{\varepsilon_1^2(\omega)+\varepsilon_2^2(\omega)}}{2}} \tag{5}$$

where $\varepsilon_1(\omega)$ & $\varepsilon_2(\omega)$ are the real and imaginary part of the frequency-dependent dielectric function, obtained from G_0W_0 + BSE.

3. Results and discussion

3.1. Structure, stability and electronic properties

Blue-AsP, also known as β-AsP, exhibits a layered structure in its bulk form and can be readily delaminated to yield a 2D monolayer characterized by an undisturbed buckled arrangement mirroring its bulk configuration. This has been ascertained by calculating the exfoliation energy, E_{exf} = 24.41 meV Å^{-2}, in line with the reference[54] using the bulk counterpart of blue-AsP (taken from the OQMD database[55]) and comparable to other layered 2D materials, such as graphene (21 meV Å^{-2}), MoS_2 (18 meV Å^{-2}), hBN (28 meV Å^{-2}) and phosphorene (22 meV Å^{-2}).[54] The optimized β-AsP is structurally analogous to blue-phosphorene with lattice parameters, $a = b$ = 3.45 Å and buckling height, h = 1.32 Å belongs to the $P3m1$ space group and therefore has a hexagonal honeycomb lattice, as shown in Fig. 1(a)–(c). The bond As–P stretches to 2.39 Å and the angle As–P–As and P–As–P bend to 92.45° which are in agreement with the previous available data.[56] The dynamical, mechanical and thermodynamical stabilities are ascertained before proceeding further and discussed in the ESI.†

Taking into account the all-round stability, it can be concluded that achieving blue AsP monolayers experimentally is feasible using suitable techniques.[57–60] One such method, as highlighted by Osters *et al.*, involves employing kinetic approaches like chemical vapor deposition, epitaxy, and solution-based routes.[60] Furthermore, the well-stable blue-AsP is found to be a wide band gap semiconductor with an indirect band gap (E_g = 2.51 eV, with HSE06; E_g = 2.95 eV with GW_0). Its valence band maximum (VBM) is located at the Γ point, while the conduction band minimum (CBM) resides between the Y and Γ points as can be seen in Fig. 1(e). The partial density of states has been calculated to understand the orbital contribution and bonding nature. The orbitals of As and P overlap, forming a strong covalent bond due to hybridization, as evident from Fig. 1(f) and the electron localization function (ELF) plot in Fig. 1(d).

3.2. Effect of lattice and temperature on the band gap

The quasiparticle band gap is determined by employing the GW approximation, which involves the first-order perturbative expansion of the electronic self-energy in relation to the screened interaction W, $\Sigma^{\mathrm{GW}} = iG(x_1,x_2)W(x_1^{\dagger},x_2)$ and including the FAN correction (eqn (1)) within the framework of AHC. This enables us to determine the temperature-dependent adjustment of the electronic energies in their bare state, influenced by the perturbation caused by the phonon field. The interaction of an electron with the lattice produces a shift in the energy levels, resulting in a temperature dependent band gap. This effect is especially important for materials with an indirect band gap, where phonons bridge the momentum gap during excitations, electron–hole formation, and recombination. The interactions between lattice vibration modes (phonons) and itinerant electrons induce transient quasiparticle excitations and weaken the Coulombic interaction between electrons and nuclei, consequently compressing the band gap (E_g).

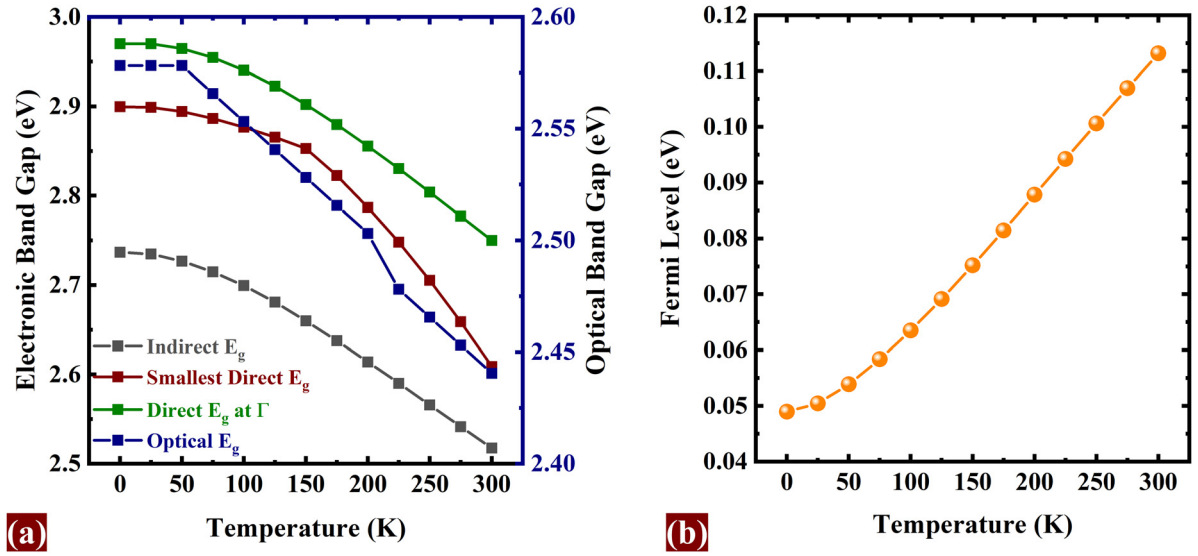

Fig. 2 (a) Electronic and optical band gap decreases with temperature, and (b) Fermi level rises with increase in temperature.

Fig. 2(a) presents the shift in electronic (indirect E_g (E_g^i), smallest direct E_g (E_g^{sd}), direct E_g at Γ ($E_g^{\Gamma d}$)) and optical E_g with temperature. Both the electronic and optical band gaps exhibit a proportional decrease with increasing temperature. The EPI-corrected electronic band gaps, which are E_g^i = 2.74 eV, E_g^{sd} = 2.90 eV, $E_g^{\Gamma d}$ = 2.97 eV at T = 0 K, drop to E_g^i = 2.52 eV, E_g^{sd} = 2.61 eV, $E_g^{\Gamma d}$ = 2.75 eV at T = 300 K, while the optical band gap 2.58 eV falls down to 2.44 eV from T = 0 K to T = 300 K. The decrease in band gap is consistent with typical temperature dependence observed in prior experimental reports.[61–63] The rise in the Fermi level with increasing temperature, as shown in Fig. 2(b), indicates that the intrinsic charge carrier concentration is increasing. Such an effect may arise from the thermal excitation of electrons from donor or acceptor states into the conduction or valence band, and could, as a result, facilitate easier photocatalysis.

3.3. Role of the catalyst in photocatalysis

A catalyst plays a crucial role by serving as a source of photogenerated charge carriers (PCC) when exposed to light, facilitating the overall reaction. These PCCs are utilized in terms of potential required for the water redox reaction. The potential generated by photogenerated electrons (U_e) support the hydrogen half reaction and is determined by measuring the distance between the CBM and the hydrogen reduction potential on an energy scale. Analogously, the potential generated by photogenerated holes (U_h) supports the oxygen half reaction and is determined by measuring the distance between the VBM and the hydrogen reduction potential on an energy scale. U_e and U_h can be adjusted with respect to different pH, by the relations: U_e(pH) = U_e(pH = 0) − 0.059 × pH and U_h(pH) = U_h(pH = 0) + 0.059 × pH in reference to the absolute vacuum scale. In our case, an intrinsic potential is supplied by the photogenerated holes and electrons for the OER and HER respectively, which is (U_h = 1.852 V, U_e = 0.646 V) in acidic media (pH = 0) while (U_h = 2.185 V, U_e = 0.276 V) in neutral media (pH = 7), effectively reducing the external bias needed to facilitate the overall water splitting reaction. These PCC potentials can also be tuned by applying external strain to the system, as evident from Fig. S4 (ESI†). U_h, specifically, is highly mutable with strain that may further minimise the need for an additional bias voltage under minute tensile strain. We have conducted additional investigations into the two half reactions under both acidic and neutral conditions in the presence of light.

An intriguing observation is that the utilization of photogenerated charge carrier (PCC) potentials significantly reduces the overpotential requirement for the oxygen evolution reaction (OER). Based on the analysis of the Gibbs free energy calculation presented in Table S1 in the ESI,† it is evident that reaction step R3 functions as the rate-determining step for the oxygen evolution reaction (OER) in both acidic and neutral media, where a minimal overpotential of 0.13 V is required in acidic media, while no overpotential is needed in neutral media. This finding highlights the effectiveness of PCC in minimizing the energy input needed for photocatalytic water splitting in different electrolyte environments.

3.4. Temperature dependent optical responses

Optical spectra delineate the distribution of light intensity as a function of wavelength or frequency, offering insights about the interaction between light and matter. The optical absorption, refractive index, extinction coefficient, and joint density of states (JDOS) describing the allowed optical transitions and often referred to as the ''fingerprints of the material'', are all dependent on the full spectrum dielectric function $\varepsilon(\omega) = \varepsilon_1(\omega) + i\varepsilon_2(\omega)$. Therefore, we have studied the temperature-dependent real and imaginary part of the frequency-dependent dielectric function, $\varepsilon_1(\omega)$ & $\varepsilon_2(\omega)$, as shown in Fig. 3(a) and (b). There is a red-shifting of the peaks in the real and imaginary part of the dielectric function, consistent with previous studies.[16,64]

In a previous study,[65] it was observed that the lattice vibration intensifies with rising temperature. This increased atomic

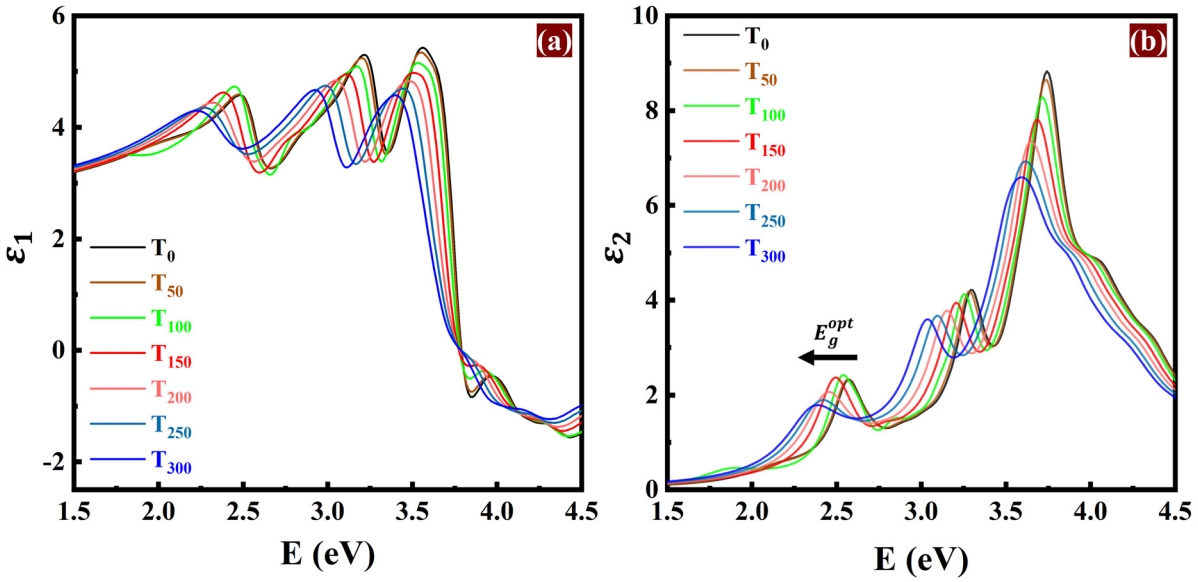

Fig. 3 Temperature-dependent (a) real [$\varepsilon_1(\omega)$] and (b) imaginary [$\varepsilon_2(\omega)$] part of the frequency-dependent dielectric function.

motion (lattice vibration) disrupts the movement of electrons *via* electron–phonon coupling, leading to a decrease in the coherence lifetimes (τ_c). Additionally, the broader spread of electron energies caused by the stronger vibrations increases the linewidth (W) of the electronic bands, which explains the observed broadening of the absorption peaks (Fig. 4(a)). To quantify this effect, we have calculated the linewidth and coherence lifetime at different temperatures, as shown in Fig. 4(e). The broader linewidth suggests decreased coherence lifetime, while the narrower linewidth corresponds to increased coherence lifetime. Red-shifting of the first absorption peak in Fig. 4(a) confirms the narrowing of the optical band gap, as detailed previously in Section 3.2. The effective utilization of light wavelengths by the photocatalyst is determined by its absorption spectrum. With increasing temperature, blue AsP remains a good absorber of photons in the visible and UVA range, where solar radiation is most abundant.

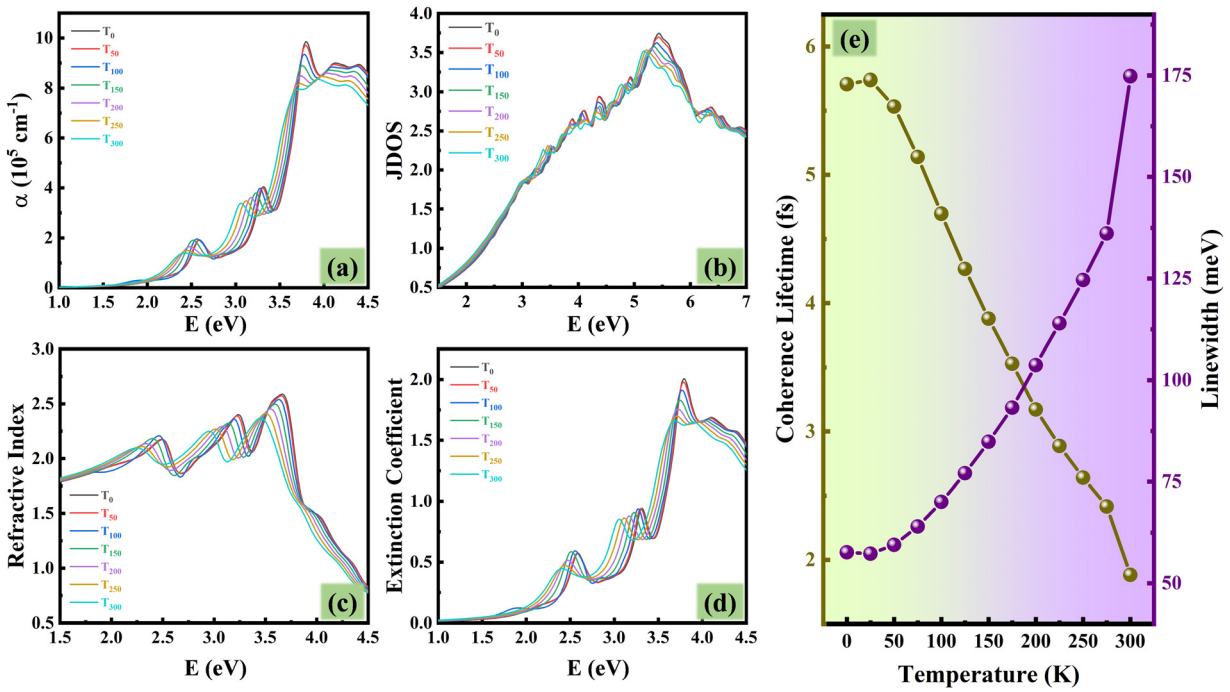

Fig. 4 Optical responses as a function of photon energy at different temperatures: (a) optical absorption coefficient (α), (b) joint density of states (JDOS), (c) refractive index, (d) extinction coefficient, and (e) coherence lifetime and linewidth.

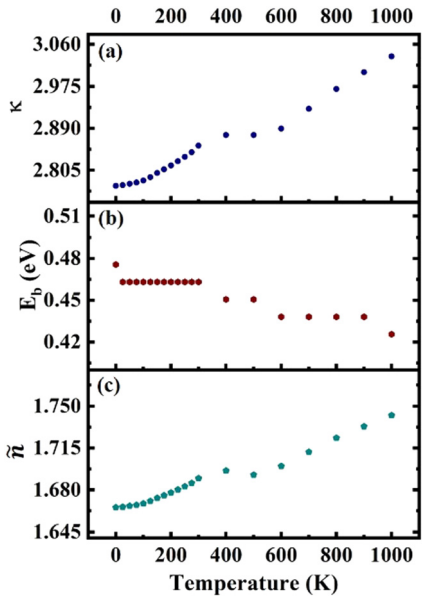

Fig. 5 (a) Static dielectric constant (κ), (b) ground state exciton binding energy (E_b), and (c) static refractive index ($\tilde{n}$).

The JDOS function suggests a slight decrease in the allowed optical transitions between occupied electronic states in the valence band and unoccupied states in the conduction band at higher temperatures in the ultraviolet (UV) region, and shows a steady rise in the number of possible electron transitions in the visible range in the optical spectrum (Fig. 4(b)). The refractive index (n) and extinction coefficient (κ) measure the extent of light bending and light absorption by the photocatalyst material per unit distance, respectively.

The refractive index quantifies how much light slows down when passing through a material compared to its speed in a vacuum. The extinction coefficient contributes to the determination of the material's optical density. A higher extinction coefficient indicates a greater ability to absorb light. Typically, an increase in temperature results in a red shift in the peak intensities of all optical spectra (Fig. 4), consistent with the dielectric response in Fig. 3. However, when we examine the y-axis (Fig. 3 and 4) between the peak intensities at a certain energy, say 3.0 eV, a consistent increase can be seen across all optical responses with rising temperature. This is due to the signature effect of temperature, the broadened peaks, attributed to the structure disorder induced by stronger electron–phonon interactions.

3.5. Effective dielectric and exciton binding energy

To effectively drive the water splitting reaction, the electron–hole pairs (excitons) need to dissociate into free charge carriers, which are then responsible for the oxidation of water to oxygen and the reduction of water to hydrogen. A low exciton binding energy facilitates the dissociation of excitons into free charge carriers, enhancing the overall efficiency of the photocatalytic process. This is because weakly bound excitons are more susceptible to thermal dissociation, allowing them to readily generate free charge carriers at the photocatalyst surface. These free charge carriers can then participate in the redox reactions involved in water splitting. Therefore, achieving a low exciton binding energy is a key factor in designing efficient photocatalysts for water splitting. The affected optical spectra and quasiparticle band gap also alter the EBE. A decrease in ground state exciton binding energy is observed (Fig. 5(b)) with increasing temperature, which can be attributed to the increased thermal energy due to electron–phonon coupling (EPC), where increased lattice vibrations (phonons) at higher temperatures enhance the rate of exciton dissociation. EPC facilitates energy transfer between excitons and phonons, weakening the Coulombic attraction between the bound electron and hole, ultimately leading to a decrease in EBE.

The static dielectric constant (Fig. 5(a)) and static refractive index (Fig. 5(c)) are increasing with increasing temperature. Higher dielectric constants, which indicate stronger polarization, tend to screen out the Coulombic interaction between charges, resulting in easier separation of charges generated by light absorption, potentially reducing charge recombination rates and enhancing the efficiency of charge transfer processes. Higher refractive index signifies reduced transparency for light, indicating that light is more likely to being refracted or scattered rather than directly transmitted through it.

The observation of excitons can sometimes be hindered by their temperature-dependent stability. However, we can estimate the maximum temperature at which exciton observation remains feasible. The minimum thermal energy required to dissociate an exciton, termed the binding energy (E_b), is equal to k_BT, where k_B is the Boltzmann constant. In this specific case, with an E_b of $\sim$0.42–0.48 eV, the maximum temperature up to which excitons can be observed will be $\sim$4900–5500 K. This significantly exceeds room temperature ($\approx$300 K), suggesting that thermal instability need not be a significant obstacle for exciton observation at typical experimental temperatures.

3.6. Dark and bright excitons

Strong coulomb effects in two-dimensional systems lead to the formation of bright and dark excitons. A bright exciton is formed when an electron jumps from the valence band to the conduction band *via* a single photon absorption. On the other hand, dark excitons involve an indirect pathway where the electron transition is assisted by phonon scattering. The bright excitons readily interact with light and are crucial for absorbing light, whereas the dark excitons, despite their slower decay, offer exciting potential in areas like quantum information processing, Bose–Einstein condensation, and light-to-energy conversion due to their extended lifetime. At room temperature (T = 300 K), two dark excitons exist lower in energy than the first bright exciton. These dark excitons cannot be directly detected through absorption spectroscopy because they do not have a corresponding peak in the spectrum, as illustrated in Fig. 6(a).

The population of bright excitons decreases at high temperature, while that of dark excitons increases (Fig. 6(b) and (c)). From a general perspective and limited understanding, it may appear that the decreasing number of bright excitons

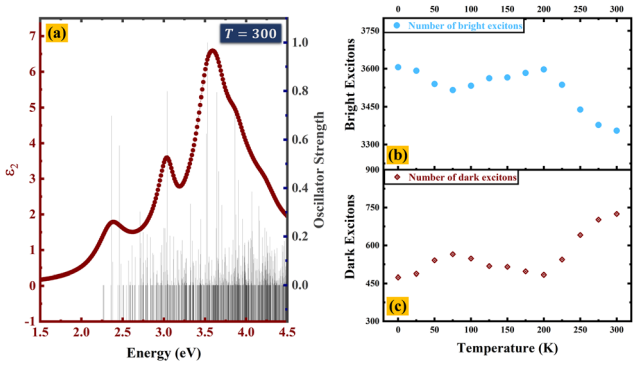

Fig. 6 (a) Imaginary dielectric constant and oscillator strength at T = 300 K, and population of (b) bright excitons and (c) dark excitons with respect to temperature.

would reduce the photocatalytic efficiency. However, interestingly, a high population of dark excitons can support photocatalysis, as discussed below.

Fig. 7 illustrates the frequency-dependent recombination and oscillator strength rate at various temperatures (T = 0 K, 100 K, 200 K and 300 K). Several observations can be made from this illustration. First of all, the first bright exciton shifts to a lower energy with increases in temperature.

Additionally, dark excitons exhibit reduced recombination rates compared to bright excitons, resulting in significantly longer lifetimes. The recombination rates are calculated using the BSE approach with Fermi's golden rule[66] and the effective exciton lifetime is calculated using a recent approach developed by Chen and Palummo.[67–69] This approach is effectively used in recent studies on top of both the Wannier approach and BSE approach using Fermi's golden rule.[36,70,71] The detailed formalism is given in the ESI.†

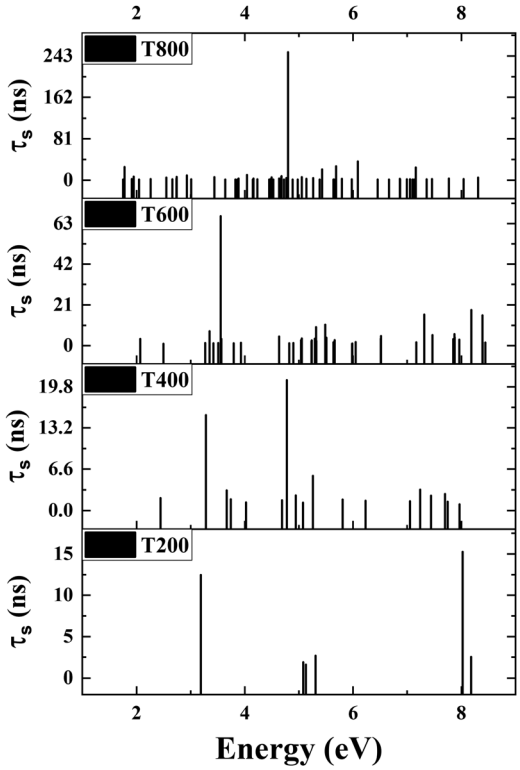

Fig. 8 Excitons with lifetimes greater than 1 ns at T = 200 K, T = 400 K, T = 600 K, T = 800 K from bottom to top.

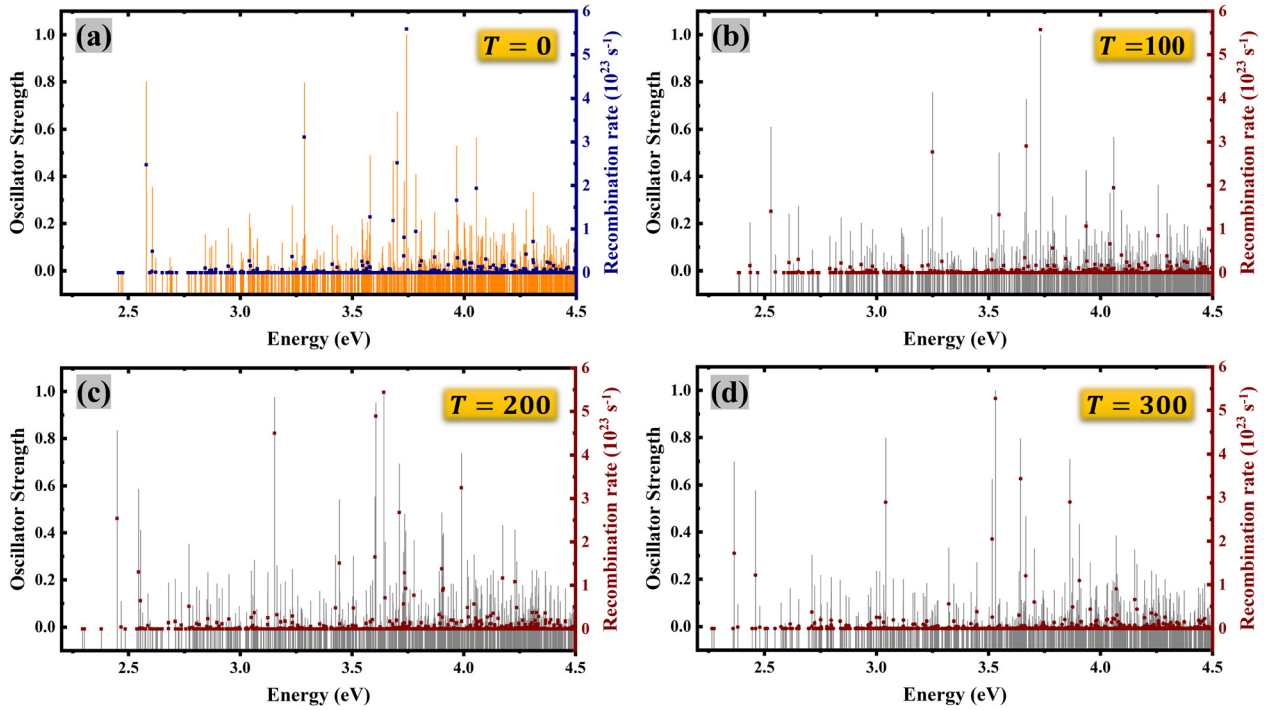

Fig. 7 Frequency-dependent oscillator strength and recombination rate at (a) T = 0 K, (b) T = 100 K, (c) T = 200 K, and (d) T = 300 K.

Dark exciton population rises with temperature, while their recombination remains significantly slower compared to bright excitons. Implication of dark excitons in photocatalysis due to their elongated lifetimes is suggested in a recent work.[70] We have used a thermal ensemble of only dark excitons and calculated the effective lifetime (τ_s) in the UV-visible region, and the excitons with $\tau_s > 1$ ns are shown in Fig. 8. The number of long-lived excitons (>1 ns) increases with temperature. Additionally, these excitons exhibit longer lifetimes at higher temperatures, reaching ~0.243 μs at 800 K. This implies that higher temperatures promote the existence of long-lived excitons. This high lifetime increases the probability of the electron–hole pair to survive long enough to reach the surface, where it can drive the redox reactions essential for photocatalytic water splitting. It is important to note here that this observation is not in contradiction with earlier understanding of decreasing coherence lifetime with increased temperature. The lifetime of bright excitons indeed decreases with increasing temperature and therefore the role of dark states in PWS becomes more important.

High-temperature photocatalysis is a promising method for splitting water into hydrogen fuel.[72,73] For the practical utilization of the β-AsP monolayer at high temperatures, we demonstrate its efficacy as a thermally stable photocatalyst by employing *ab initio* molecular dynamics (AIMD) simulations at room temperature (T = 300 K) and above (T = 500 K, 800 K) with a time step of 1 fs over a duration of 5 ps. The β-AsP monolayer maintained its structural integrity throughout the simulations, as shown in Fig. S3 of the ESI.† This suggests promising thermal stability for applications in high-temperature photocatalysis.

3.7. Photocatalytic water splitting

A wide band gap holds significant allure for photocatalytic water splitting if it adheres to thermodynamic favourability. For that, the band edges must straddle the standard water redox potentials, $E^{\mathrm{Red}}_{\mathrm{H^+/H_2}} = -4.44 + \mathrm{pH} \times 0.0529$ eV and $E^{\mathrm{Ox}}_{\mathrm{O_2/H_2O}} = -5.67 + \mathrm{pH} \times 0.0529$ eV in the absolute vacuum scale (AVS). β-AsP not only adheres to the thermodynamic favourability but also appears to be an efficient photocatalyst with substantial photogenerated holes and electrons (refer to Fig. S4 in ESI†), which can significantly reduce the free energy for the photocatalytic water splitting. This has been observed in both neutral (pH = 7) and acidic (pH = 0) media.

The process of water splitting, which involves the dissociation of water molecules into H^+ and OH^- ions and their subsequent conversion into H_2 and O_2, occurs through a series of intricate atomic-level mechanisms. To begin with, the water splitting reaction can be analysed as two half reactions: the hydrogen evolution reaction (HER) and oxygen evolution reaction (OER). The HER proceeds in two steps, while the OER

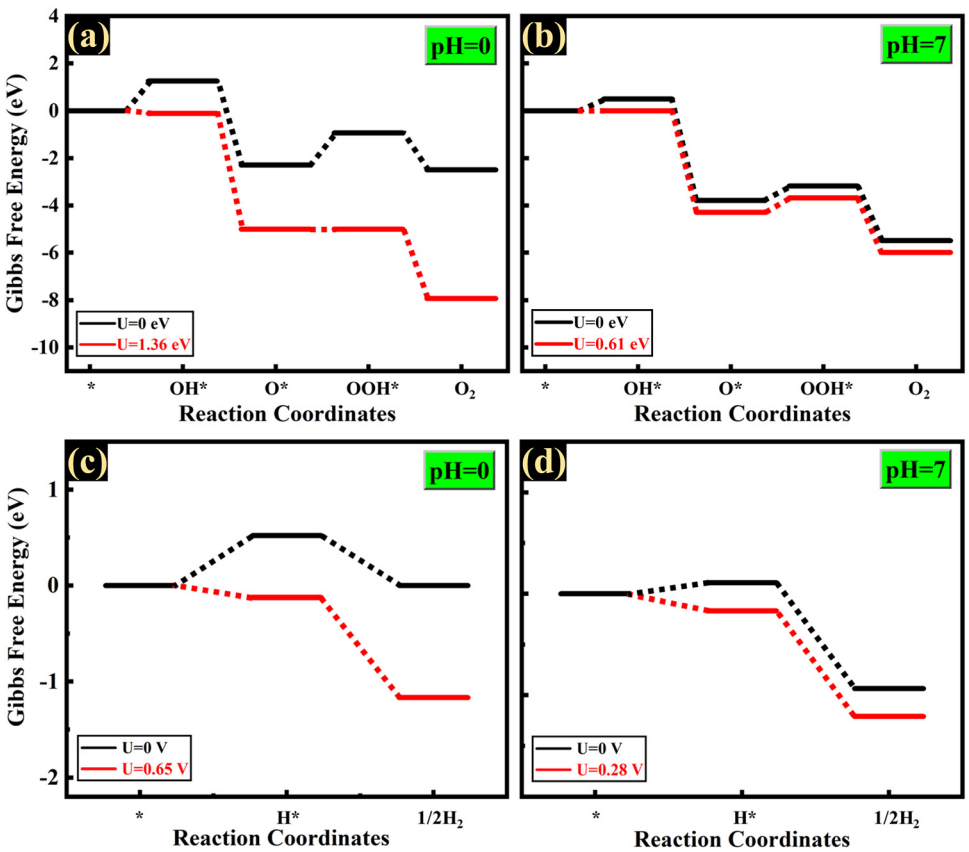

Fig. 9 Gibbs free energy for the oxygen evaluation reaction (OER) and hydrogen evaluation reaction (HER) at (a) and (c) pH = 0, and (b) and (d) pH = 7.

involves four steps (see the details in ESI†). In the presence of a catalyst, these evolution reactions take place at the catalyst-water interface.

The buckled structure of AsP confers it with notable benefits as a photocatalyst, making it suitable for facilitating the hydrogen evolution reaction (HER) on the phosphorus site and the oxygen evolution reaction (OER) on the arsenic site. To ascertain the active sites for the HER and OER, we have calculated the Gibbs' free energy profile at both the sites for the HER and OER. The overpotential required for the OER at the phosphorus (P) site is 1.15 eV, while that at the arsenic (As) site is just 0.13 eV. Then, the overpotential needed for the HER at the As site is 0.12 eV, whereas no overpotential is required at the P site. Therefore, the energetics favour the phosphorus site for the HER and the arsenic site for the OER. The externally required potential necessary for the OER amounts to a mere 0.61 V (1.36 V) at pH = 7 (pH = 0), which is lower than that of $SiCP_2$ (0.85 V), $CdPSe_3$ (1.36 V), and $ZnPSe_3$ (1.30 V),[74,75] and lies in the range of those of many transition metal carbides and oxides (0.49–1.70 V).[76] It offers the distinct advantage of avoiding the reliance on precious metals such as ruthenium and iridium, thereby sidestepping the challenges associated with their scarcity and high cost.[77] Interestingly, the intrinsic potential supplied by the photogenerated electrons ($U_{e(pH=0)}$ = 0.646 V, $U_{e(pH=7)}$ = 0.276 V) is sufficient to drive the HER reaction without any external biasing, both in acidic and neutral media. Therefore, β-AsP demonstrates its efficiency as a photocatalyst capable of directly producing H_2 from pure water (pH = 7) and acidic water (pH = 0) under visible light exposure without requiring sacrificial reagents or cocatalysts. The Gibbs free energy profiles for the OER and HER are given in Fig. 9 and the details of the calculation are given in the ESI.† Additionally, highly anisotropic charge carrier mobilities in blue-AsP contribute to efficient charge transfer and the separation of photoinduced electron–hole pairs, as detailed in the ESI.†

4. Conclusion

In summary, the effect of temperature on the electronic and optical responses is prominent due to electron-lattice interaction. With a 10^6 cm^{-1} absorption coefficient, β-AsP shines as a photocatalyst, producing H_2 from both clean (pH = 7) and acidic water (pH = 0) under visible light without the need for cocatalysts or sacrificial reagents. By meticulously incorporating electron–electron correlation, electron–hole interaction and electron–phonon coupling employing the robust Allen–Heine–Cardona (AHC) formalism atop GW + BSE simultaneously, we have demonstrated that the efficiency of photocatalytic water splitting will be enhanced at high temperature with the aid of several key factors: a narrowed band gap, reduced exciton binding energy, a lower recombination rate, and a longer exciton lifetime. Importantly, the presence of abundant ''dark'' excitons at high temperatures with extended lifetimes significantly contributes to the increased photocatalytic efficiency. This study constitutes a bedrock to envisage the comprehensive understanding of the temperature-dependent excitonic perspective in photocatalysis and other optoelectronic properties.

Data availability

The data that support the findings of this study are available from the authors upon reasonable request.

Conflicts of interest

The authors declare no conflict of interest.

Acknowledgements

The authors extend their heartfelt gratitude to the Institute of Nano Science and Technology (INST) in Mohali, PARAM-Smriti at NABI, Mohali and C-DAC in Pune for providing the supercomputing resources under the umbrella of the National Supercomputing Mission, by the Government of India. Additionally, the authors are deeply thankful for the fellowship and financial assistance provided by INST Mohali and the Council of Scientific and Industrial Research (CSIR), India, under grant number 09/1129(0030)/2020-EMR-I. Support from Project No. CRG/2023/001896 of Science and Engineering Research Board – Department of Science & Technology (SERB-DST), Govt. of India is gratefully acknowledged.

References

1 Z. Wang, D. Kortge, Z. He, J. Song, J. Zhu, C. Lee, H. Wang and P. Bermel, Selective emitter materials and designs for high-temperature thermophotovoltaic applications, *Sol. Energy Mater. Sol. Cells*, 2022, **238**, 111554.
2 N. Zhou, X. Xu, A. T. Hammack, B. C. Stipe, K. Gao, W. Scholz and E. C. Gage, Plasmonic near-field transducer for heat-assisted magnetic recording, *Nanophotonics*, 2014, **3**, 141–155.
3 N. P. Padture, M. Gell and E. H. Jordan, Thermal Barrier Coatings for Gas-Turbine Engine Applications, *Science*, 2002, **296**, 280–284.
4 R. Zhang, H. Wang, X. Peng, R. R. Feng, A. A. Liu, Q. Guo, C. Zhou, Z. Ma, X. Yang, Y. Jiang and Z. Ren, In Situ Studies on Temperature-Dependent Photocatalytic Reactions of Methanol on TiO2(110), *J. Phys. Chem. C*, 2019, **123**, 9993–9999.
5 F. Meng, Y. Liu, J. Wang, X. Tan, H. Sun, S. Liu and S. Wang, Temperature dependent photocatalysis of g-C_3N_4, TiO_2 and ZnO: Differences in photoactive mechanism, *J. Colloid Interface Sci.*, 2018, **532**, 321–330.
6 E. Nurlaela, T. Shinagawa, M. Qureshi, D. S. Dhawale and K. Takanabe, Temperature Dependence of Electrocatalytic and Photocatalytic Oxygen Evolution Reaction Rates Using NiFe Oxide, *ACS Catal.*, 2016, **6**, 1713–1722.
7 M. Matsuoka, Y. Ide and M. Ogawa, Temperature-dependent photocatalytic hydrogen evolution activity from

water on a dye-sensitized layered titanate, *Phys. Chem. Chem. Phys.*, 2014, **16**, 3520–3522.
8 G. Strinati, Application of the Green's functions method to the study of the optical properties of semiconductors, *La Riv. Del Nuovo Cim. Ser. 3*, 1988, **11**, 1–86.
9 P. B. Allen and M. Cardona, Temperature dependence of the direct gap of Si and Ge, *Phys. Rev. B: Condens. Matter Mater. Phys.*, 1983, **27**, 4760.
10 M. Cardona, Electron–phonon interaction in tetrahedral semiconductors, *Solid State Commun.*, 2005, **133**, 3–18.
11 H. Reddy, U. Guler, A. V. Kildishev, A. Boltasseva and V. M. Shalaev, Temperature-dependent optical properties of gold thin films, *Opt. Mater. Express*, 2016, **6**(9), 2776–2802.
12 H. G. Liljenvall and A. G. Mathewson, The optical properties of silver in the energy range 3.2–4.3 eV as a function of temperature, *J. Phys. C-Solid State Phys.*, 1970, **3**, S341.
13 A. M. Brown, R. Sundararaman, P. Narang, W. A. Goddard and H. A. Atwater, Ab initio phonon coupling and optical response of hot electrons in plasmonic metals, *Phys. Rev. B*, 2016, **94**, 075120.
14 H. Reddy, U. Guler, K. Chaudhuri, A. Dutta, A. V. Kildishev, V. M. Shalaev and A. Boltasseva, Temperature-Dependent Optical Properties of Single Crystalline and Polycrystalline Silver Thin Films, *ACS Photonics*, 2017, **4**, 1083–1091.
15 G. Cassabois, G. Fugallo, C. Elias, P. Valvin, A. Rousseau, B. Gil, A. Summerfield, C. J. Mellor, T. S. Cheng, L. Eaves, C. T. Foxon, P. H. Beton, M. Lazzeri, A. Segura and S. V. Novikov, Exciton and Phonon Radiative Linewidths in Monolayer Boron Nitride, *Phys. Rev. X*, 2022, **12**, 011057.
16 Z. Han, C. Lee, J. Song, H. Wang, P. Bermel and X. Ruan, Temperature-dependent full spectrum dielectric function of semiconductors from first principles, *Phys. Rev. B*, 2023, **107**, L201202.
17 H. Kawai, K. Yamashita, E. Cannuccia and A. Marini, Electron-electron and electron-phonon correlation effects on the finite-temperature electronic and optical properties of zinc-blende GaN, *Phys. Rev. B: Condens. Matter Mater. Phys.*, 2014, **89**, 085202.
18 H. G. Park, T. J. Kim, F. Ullah, V. L. Le, H. T. Nguyen, Y. S. Kim and Y. D. Kim, Temperature Dependence of the Dielectric Function of Monolayer $MoSe_2$, *Sci. Rep.*, 2018, **8**(1), 1–10.
19 S. Poncé, G. Antonius, Y. Gillet, P. Boulanger, J. Laflamme Janssen, A. Marini, M. Côté and X. Gonze, Temperature dependence of electronic eigenenergies in the adiabatic harmonic approximation, *Phys. Rev. B: Condens. Matter Mater. Phys.*, 2014, **90**, 214304.
20 X. Cai, Y. Chen, B. Sun, J. Chen, H. Wang, Y. Ni, L. Tao, H. Wang, S. Zhu and X. Li, *et al.*, Two-dimensional Blue-AsP monolayers with tunable direct band gap and ultrahigh carrier mobility show promising high-performance photovoltaic properties, *Nanoscale*, 2019, **11**, 8260–8269.
21 H. Zhao, B. Jia, X. Guan, Y. Chen, X. Zhu, L. Han and P. Lu, A promising type-II β-AsP/g-C6N6 van der Waals heterostructure photocatalyst for water splitting: a first-principles study, *Phys. Chem. Chem. Phys.*, 2022, **24**, 24939–24949.
22 H. Zhao, B. Jia, Z. Wang, L. Han, H. Song and P. Lu, High-efficiency hydrogen evolution reaction photocatalyst for water splitting of Type-II β-AsP/g-C3N4 van der Waals heterostructure, *Int. J. Hydrogen Energy*, 2023, **48**, 10051–10061.
23 H. Guo, B. Zhu, F. Zhang, H. Li, K. Zheng, J. Qiu, L. Wu, J. Yu and X. Chen, Type-II AsP/Sc_2CO_2 van der Waals heterostructure: an excellent photocatalyst for overall water splitting, *Int. J. Hydrogen Energy*, 2021, **46**, 32882–32892.
24 H. Zhao, Q. Wang, B. Jia, L. Han, W. Chen, J. Hao, L. Wu, P. Lu and P. Guan, Quasiparticle energies and significant exciton effects of monolayered blue arsenic phosphorus conformers, *Phys. Chem. Chem. Phys.*, 2021, **23**, 23808–23817.
25 J. Zhang, Y. F. Zhang, Y. Li, Y. R. Ren, S. Huang, W. Lin and W. K. Chen, Blue-AsP monolayer as a promising anode material for lithium- and sodium-ion batteries: a DFT study, *Phys. Chem. Chem. Phys.*, 2021, **23**, 5143–5151.
26 N. Khossossi, V. Shukla, Y. Benhouria, I. Essaoudi, A. Ainane, R. Ahuja, G. Babu and P. M. Ajayan, Exploring the Possibility of β-Phase Arsenic-Phosphorus Polymorph Monolayer as Anode Materials for Sodium-Ion Batteries, *Adv. Theory Simul.*, 2020, **3**, 2000023.
27 Y. Mao, C. Qin, X. Zhou, Z. Zhang and J. Yuan, First-principles study on GeC/β-AsP heterostructure with type-II band alignment for photocatalytic water splitting, *Appl. Surf. Sci.*, 2023, **617**, 156298.
28 Z. Wang, X. Wei, Y. Huang, J. Zhang and J. Yang, High solar-to-hydrogen efficiency in AsP/GaSe heterojunction for photocatalytic water splitting: A DFT study, *Mater. Sci. Semicond. Process.*, 2023, **159**, 107393.
29 S. Ahmed, X. Cai, M. M. E. Ali and H. Wang, Exploring the adsorption characteristics of toxic CO gas on pristine, defective, and transition metal-doped I-AsP monolayer, *Comput. Theor. Chem.*, 2024, **1232**, 114464.
30 F. Liu, J. Xue, Q. Yu, B. Shu, Y. Lu, Y. Dai, X. Pang, H. Deng, X. Wang, S. Zhu, J. Wu and T. He, Recent advances in stable arsenic–phosphorus: preparation, properties, and application, *J. Phys. D: Appl. Phys.*, 2022, **55**, 453001.
31 H. Seksaria, A. Kishore and A. De Sarkar, Probing 2D Exciton Dynamics of Non-Hydrogenic Anisotropic Rydberg Spectra in Anomalous Screening Regime, *J. Phys. Chem. C*, 2024, **128**, 42.
32 L. Hu, C. Xu, L. Peng, F. L. Gu and W. Yang, Photocatalytic activity and the radiative lifetimes of excitons via an ab initio approach, *J. Mater. Chem. A*, 2018, **6**, 15027–15032.
33 B. Ohtani, Titania Photocatalysis beyond Recombination: A Critical Review, *Catalysts*, 2013, **3**, 942–953.
34 B. Miller, A. Steinhoff, B. Pano, J. Klein, F. Jahnke, A. Holleitner and U. Wurstbauer, Long-Lived Direct and Indirect Interlayer Excitons in van der Waals Heterostructures, *Nano Lett.*, 2017, **17**, 5229–5237.
35 D. Unuchek, A. Ciarrocchi, A. Avsar, K. Watanabe, T. Taniguchi and A. Kis, Room-temperature electrical control of exciton flux in a van der Waals heterostructure, *Nature*, 2018, **560**(7718), 340–344.

36 H. Seksaria, A. Kaur, K. Singh and A. De Sarkar, Hexagonal and tetragonal ScX (X = P, As, Sb) nanosheets for optoelectronics and straintronics, *Appl. Surf. Sci.*, 2023, **615**, 156306.
37 H. Y. Chen, D. Sangalli and M. Bernardi, First-principles ultrafast exciton dynamics and time-domain spectroscopies: Dark-exciton mediated valley depolarization in monolayer WSe_2, *Phys. Rev. Res.*, 2022, **4**, 043203.
38 P. Hohenberg and W. Kohn, Inhomogeneous electron gas, *Phys. Rev.*, 1964, **136**, B864.
39 G. Kresse and J. Furthmüller, Efficiency of ab-initio total energy calculations for metals and semiconductors using a plane-wave basis set, *Comput. Mater. Sci.*, 1996, **6**, 15–50.
40 G. Kresse and J. Furthmüller, Efficient iterative schemes for ab initio total-energy calculations using a plane-wave basis set, *Phys. Rev. B: Condens. Matter Mater. Phys.*, 1996, **54**, 11169.
41 G. Kresse and D. Joubert, From ultrasoft pseudopotentials to the projector augmented-wave method, *Phys. Rev. B: Condens. Matter Mater. Phys.*, 1999, **59**, 1758.
42 J. P. Perdew, K. Burke and M. Ernzerhof, Generalized Gradient Approximation Made Simple, *Phys. Rev. Lett.*, 1996, **77**, 3865.
43 A. V. Krukau, O. A. Vydrov, A. F. Izmaylov and G. E. Scuseria, Influence of the exchange screening parameter on the performance of screened hybrid functionals, *J. Chem. Phys.*, 2006, **125**, 224106.
44 A. Togo and I. Tanaka, First principles phonon calculations in materials science, *Scr. Mater.*, 2015, **108**, 1–5.
45 P. Giannozzi, S. Baroni, N. Bonini, M. Calandra, R. Car, C. Cavazzoni, D. Ceresoli, G. L. Chiarotti, M. Cococcioni and I. Dabo, *et al.*, QUANTUM ESPRESSO: a modular and open-source software project for quantum simulations of materials, *J. Phys.: Condens. Matter*, 2009, **21**, 395502.
46 D. R. Hamann, M. Schlüter and C. Chiang, Norm-Conserving Pseudopotentials, *Phys. Rev. Lett.*, 1979, **43**, 1494.
47 D. R. Hamann, Optimized norm-conserving Vanderbilt pseudopotentials, *Phys. Rev. B: Condens. Matter Mater. Phys.*, 2013, **88**, 085117.
48 A. F. Starace, Length and Velocity Formulas in Approximate Oscillator-Strength Calculations, *Phys. Rev. A: At., Mol., Opt. Phys.*, 1971, **3**, 1242.
49 D. Sangalli, A. Ferretti, H. Miranda, C. Attaccalite, I. Marri, E. Cannuccia, P. Melo, M. Marsili, F. Paleari and A. Marrazzo, *et al.*, Many-body perturbation theory calculations using the yambo code, *J. Phys.: Condens. Matter*, 2019, **31**, 325902.
50 A. Marini, C. Hogan, M. Grüning and D. Varsano, yambo: An ab initio tool for excited state calculations, *Comput. Phys. Commun.*, 2009, **180**, 1392–1403.
51 P. B. Allen and V. Heine, Theory of the temperature dependence of electronic band structures, *J. Phys. C-Solid State Phys.*, 1976, **9**, 2305.
52 H. Y. Fan, Temperature Dependence of the Energy Gap in Semiconductors, *Phys. Rev.*, 1951, **82**, 900.
53 A. Marini, S. Poncé and X. Gonze, Many-body perturbation theory approach to the electron-phonon interaction with density-functional theory as a starting point, *Phys. Rev. B: Condens. Matter Mater. Phys.*, 2015, **91**, 224310.
54 J. H. Jung, C. H. Park and J. Ihm, A Rigorous Method of Calculating Exfoliation Energies from First Principles, *Nano Lett.*, 2018, **18**, 2759–2765.
55 J. E. Saal, S. Kirklin, M. Aykol, B. Meredig and C. Wolverton, Materials design and discovery with high-throughput density functional theory: The open quantum materials database (OQMD), *JOM*, 2013, **65**, 1501–1509.
56 J. P. Tang, W. Z. Xiao and L. L. Wang, Stability and electronic structure of two-dimensional arsenic phosphide monolayer, *Mater. Sci. Eng. B*, 2018, **228**, 206–212.
57 I. Karakaya and W. T. Thompson, The asp (arsenicphosphorus) system, *J. Phase Equilib.*, 1991, **12**, 343–346.
58 H. Krebs, W. Holz and K. H. Worms, Über die Struktur und die Eigenschaften der Halbmetalle, X. Eine Neue Rhombische Arsenmodifikation und Ihre Mischkristallbildung mit Schwarzem Phosphor, *Chem. Ber.*, 1957, **90**, 1031–1037.
59 B. Liu, M. Köpf, A. N. Abbas, X. Wang, Q. Guo, Y. Jia, F. Xia, R. Weihrich, F. Bachhuber, F. Pielnhofer and E. Al, Black Arsenic–Phosphorus: Layered Anisotropic Infrared Semiconductors with Highly Tunable Compositions and Properties, *Adv. Mater.*, 2015, **27**, 4423–4429.
60 O. Osters, T. Nilges, F. Bachhuber, F. Pielnhofer, R. Weihrich, M. Schöneich and P. Schmidt, Synthesis and identification of metastable compounds: Black arsenic - Science or fiction?, *Angew. Chem., Int. Ed.*, 2012, **51**, 2994–2997.
61 Y. Cho, A. Yamaguchi, R. Uehara, S. Yasuhara, T. Hoshina and M. Miyauchi, Temperature dependence on bandgap of semiconductor photocatalysts, *J. Chem. Phys.*, 2020, **152**, 231101.
62 Y. P. Varshni, Temperature dependence of the energy gap in semiconductors, *Physica*, 1967, **34**, 149–154.
63 M. De La Mare, Q. Zhuang, A. Krier, A. Patan and S. Dhar, Growth and characterization of InAsN/GaAs dilute nitride semiconductor alloys for the midinfrared spectral range, *Appl. Phys. Lett.*, 2009, **95**(3), DOI: **10.1063/1.3187534/132018**.
64 W. Zhang, W. Zhang, T. Fei, T. Fei, T. Cheng, T. Cheng, C. Zheng, Y. Dong, J.-Y. Yang, J.-Y. Yang, J.-Y. Yang, L. Liu, L. Liu and L. Liu, Doping and temperature-dependent UV-Vis optical constants of cubic $SrTiO_3$: a combined spectroscopic ellipsometry and first-principles study, *Opt. Mater. Express*, 2021, **11**(3), 895–904.
65 J. Y. Yang, L. H. Liu and J. Y. Tan, First-principles molecular dynamics study on temperature-dependent dielectric function of bulk 3C and 6H SiC in the energy range 3–8 eV, *Phys. B*, 2014, **436**, 182–187.
66 K. Mohammad, *Calculation of the radiative lifetime and optical properties for three-dimensional (3D) hybrid perovskites*, 2016.
67 M. Palummo, M. Bernardi and J. C. Grossman, Exciton radiative lifetimes in two-dimensional transition metal dichalcogenides, *Nano Lett.*, 2015, **15**, 2794–2800.

68 H. Y. Chen, M. Palummo, D. Sangalli and M. Bernardi, Theory and Ab Initio Computation of the Anisotropic Light Emission in Monolayer Transition Metal Dichalcogenides, *Nano Lett.*, 2018, **18**, 3839–3843.

69 H. Y. Chen, V. A. Jhalani, M. Palummo and M. Bernardi, Ab initio calculations of exciton radiative lifetimes in bulk crystals, nanostructures, and molecules, *Phys. Rev. B*, 2019, **100**, 075135.

70 M. Re Fiorentin, F. Risplendi, M. Palummo and G. Cicero, First-Principles Calculations of Exciton Radiative Lifetimes in Monolayer Graphitic Carbon Nitride Nanosheets: Implications for Photocatalysis, *ACS Appl. Nano Mater.*, 2021, **4**, 1985–1993.

71 Z. Yan, Y. Li and S. Wang, Spin Mixing Control of Interlayer Excitons in ZrS_2/ZrNCl Heterostructures, *J. Phys. Chem. C*, 2023, **127**, 20939–20944.

72 Y. Li, Y. K. Peng, L. Hu, J. Zheng, D. Prabhakaran, S. Wu, T. J. Puchtler, M. Li, K. Y. Wong, R. A. Taylor and S. C. E. Tsang, Photocatalytic water splitting by N-TiO_2 on MgO(111) with exceptional quantum efficiencies at elevated temperatures, *Nat. Commun.*, 2019, **10**(1), 1–9.

73 J. Li, L. Ding, Z. Su, K. Li, F. Fang, R. Sun, Y. Qin and K. Chang, Non-Lignin Constructing the Gas–Solid Interface for Enhancing the Photothermal Catalytic Water Vapor Splitting, *Adv. Mater.*, 2023, **35**, 2305535.

74 B. Wang, Y. Sun and G. Yang, $SiCP_4$ Monolayer with a Direct Band Gap and High Carrier Mobility for Photocatalytic Water Splitting, *J. Phys. Chem. Lett.*, 2022, **13**, 190–197.

75 A. Kishore, H. Seksaria, A. Arora and A. De Sarkar, Regulating excitonic effects in non-oxide based $XPSe_3$ (X = Cd, Zn) monolayers towards enhanced photocatalysis for overall water splitting, *Phys. Chem. Chem. Phys.*, 2023, **25**, 20337–20349.

76 J. S. Kim, B. Kim, H. Kim and K. Kang, Recent Progress on Multimetal Oxide Catalysts for the Oxygen Evolution Reaction, *Adv. Energy Mater.*, 2018, **8**, 1702774.

77 X. Cui, P. Ren, D. Deng, J. Deng and X. Bao, Single layer graphene encapsulating non-precious metals as high-performance electrocatalysts for water oxidation, *Energy Environ. Sci.*, 2016, **9**, 123–129.